Journal of Materials Chemistry C

Accepted Manuscript

This article can be cited before page numbers have been issued, to do this please use: M. Imran, S. S. A. A. H. Rashi, Y. M. Sabri, N. Motta, T. Tesfamichael, P. M. Sonar and M. Shafiei, *J. Mater. Chem. C*, 2019, DOI: 10.1039/C8TC05982A.

ROYAL SOCIETY OF CHEMISTRY

rsc.li/materials-c

View Article Online
DOI: 10.1039/C8TC05982A

Journal Name

ARTICLE

Received 00th January 20xx,

Accepted 00th January 20xx

DOI: 10.1039/x0xx00000x

www.rsc.org/

Template based Sintering of WO_3 Nanoparticles into Porous Tungsten Oxide Nanofibers for Acetone Sensing Applications

Muhammad Imran,[a] Syed Sulthan Alaudeen Abdul Haroon Rashid,[b] Ylias Sabri,[b] Nunzio Motta,[a] Tuquabo Tesfamichael,[a] Prashant Sonar,[a] and Mahnaz Shafiei *[a,c]

Porous WO_3 nanofibers have been synthesized by electrospining polyvinylpyrrolidone (PVP) nanofibers embedded with semiconducting WO_3 nanoparticles followed by annealing in air. The PVP serves as a template in sintering of WO_3 nanoparticles into nanofibrous morphology. Scanning electron microscopy (SEM) and transmission electron microscopy (TEM) characterizations have revealed highly porous structure of WO_3 nanofibers with diameter in the range of 800 – 1200 nm. Fourier transform infrared spectroscopy (FTIR) confirms complete removal of polymer from the porous WO_3 NFs after annealing. Amperometric based sensing performance of porous WO_3 nanofibers is evaluated toward low concentrations (1.8- 12.5 ppm) of acetone and further improved via light excitation (365 nm UV) and applied bias voltage (3V – 7V). The applied bias voltage has shown a significant effect on sensor characteristics with a remarkably enhanced response at higher bias voltage. A maximum response ($I_{gas} - I_{air}$) of 1.79 μA is obtained at 7 V bias voltage toward 12.5 ppm acetone at 350 °C under UV irradiation. The porous WO_3 nanofibers are able to detect 700 ppb of acetone with 3 V bias voltage using photo-activation with response/recovery time of 33 s/42 s and excellent repeatability. The experimental results confirm a potential usage of the developed sensor based on electrospun porous WO_3 nanofibers for acetone sensing applications.

Introduction

Semiconducting metal oxides (MOx) applications encompass numerous fields of science and technology such as solar cells,[1-3] photocatalysts[4, 5] and sensors for environmental and biomedical monitoring.[6-14] Among these applications, MOx utilization as gas sensing materials are escalating at rapid pace due to increased social concerns about environment pollution, security and healthcare.[15, 16] Therefore, low-cost gas sensors with exceptional sensitivity, selectivity, stability, repeatability and low response/recovery time are highly desirable for their practical implementation into the society.[17] These sensing parameters can be improved by reducing the size of sensing materials which enhance the reaction sites and specific surface area compared with thick or thin film technology. For this purpose, several types of nanomaterials including 0D,[18-20] 1D,[6, 17, 21-35] quasi 1D,[29, 36, 37] and 2D[38] have been successfully synthesized and applied for gas sensing applications. Among these nanomaterials, 1D nanomaterials have been widely applied for gas sensing owing to their unique properties including large surface to volume ratio, better charge transport properties, high specific surface area, more surface active sites as well as the effect of crystal facets with high surface reactivity.[39, 40] Nanofibers (NFs) - 1D nanomaterials - are produced by many different approaches. For example, a molten-salt method, wet (or liquid) chemistry, nano-carving, self-catalyst growth, template-assisted or sacrificial template synthesis, chemical vapour deposition, thermal evaporation, spray pyrolysis and electrospinning.[9, 41, 42] Among these techniques, electrospinning is one of the most versatile and robust techniques for synthesis of functional nanofibers with unique structure and diverse properties.[43-47] The intrinsic sensing response of the semiconducting MOx nanofibers are improved by optimizing microstructure, chemical and phase composition, shape, surface morphology, porosity (pore size and pore density), and interconnectivity of the individual fibers.[48, 49] Microstructure, surface morphology and porosity are mainly dependent on calcination parameters after the electrospinning.

[a] Institute for Future Environments and School of Chemistry, Physics, and Mechanical Engineering, Queensland University of Technology (QUT), Brisbane, QLD 4001, Australia.
[b] Centre for Advanced Materials and Industrial Chemistry (CAMIC), School of Applied Sciences, RMIT University, Melbourne, VIC 3001, Australia.
[c] Faculty of Science, Engineering and Technology, Swinburne University of Technology, Hawthorn, VIC 3122, Australia.
*Email: mshafiei@swin.edu.au

Electronic Supplementary Information (ESI) available: [Effect of electrospinning parameters on mean fiber diameter of PVP/WO_3 composite NFs; Fiber diameter distribution of PVP/WO_3 fibers electrospun at (a, a') 9 and 15 KV; (b, b') 12 and 16 cm; and (c, c') 1.2 ml/hr and 0.6 ml/hr, respectively; (a) SEM image, and (b) fiber diameter distribution of PVP/WO_3 composite NFs electrospun at 9 KV, with feed rate of 0.3 ml/hr and tip to collector distance of 16 cm. (c) SEM image (inset shows high resolution SEM image) and (d) fiber diameter distribution of porous WO_3 NFs after annealing; EDX analysis of PVP/WO_3 composite NFs; FTIR analysis of PVP/WO_3 composite NFs and porous WO_3 NFs; Temperature profile of annealing process; Annealing duration and temperature profile; SEM images of calcined WO3 nanofibers at different temperatures and stay time; XPS high resolution spectra of C 1s and substrate (Al foil); Summarized sensing behavior of porous WO_3 NFs with biased voltage of 3 V at different operating temperatures; Dynamic response of porous WO_3 NFs at (a) 250 °C; and (b) 350 °C with a bias voltage of 7 V toward acetone with different concentrations without and with UV irradiation (Dark and Light); Stability of the sensor after 7 days]. See DOI: 10.1039/x0xx00000x

View Article Online
DOI: 10.1039/C8TC05982A

Among different semiconducting MOx, WO_3 particularly has gained much attention of researchers in the field of gas sensing because of its wide band gap (2.6 – 3.0 eV) properties.[13, 14, 50-52] Intrinsic gas sensing characteristics of WO_3 have been improved by doping with different noble metals,[17] catalytic materials,[34, 52, 53] MOx[30, 33, 54] and have also been combined with various semiconducting MOxs[29] and graphene oxide (GO)[55, 56] to make composite materials. Response of WO_3 NFs based sensors toward a specific analyte gas mainly depends on grain size, specific surface area and reaction sites of the nanofibers. A higher response is expected from a material having smaller grains, nano-crystalline structure, high porosity and larger surface area.[49, 57]

Conductometric devices based on WO_3 NFs have already been developed and applied for acetone sensing applications. For example, Wei et al.[6] have developed porous WO_3 NFs using sol-gel method followed by annealing in air having a maximum response of 55.6 to 50 ppm acetone at 270 ℃ with a detection limit of 0.1 ppm. Several strategies have been developed to improve sensing performance, including functionalizing with different catalytic metals: Pt,[53, 58] Pd[34, 59] and Au nanoparticles (NPs).[17] Kim et al.[60-63] have reported MOx NFs (e.g. WO_3 and ZnO) functionalized with protein (apoferritin) encapsulated transition metal NPs exhibiting superior sensitivity, selectivity and fast response in a high humidity environment (95% relative humidity (RH)). Protein (apoferritin) encapsulation results in uniform dispersity of the catalytic NPs due to positively charged surface of apoferritin. WO_3 NFs functionalized by RuO_2[60] and Rh_2O_3[33] NPs have also shown improved response toward acetone at 350 °C. Recently, Choi et al.[64] have developed plasma treated WO_3 bumpy hemi-tube structures on GO sheets for acetone sensing. The GO-WO_3 hemi-tube structure shows a response of 3.25 toward 5 ppm acetone at 300 ℃ with a response/recovery time of ~15 s/~33 s in highly humid environment (85 – 95%RH) with a detection limit of 100 ppb. Khan et al.[14] have also reported that two dimensional WO_3 nanosheets are also promising materials for gas sensing. They have measured a high response factor of ~30 to ultralow 40 ppb NO_2 at a relatively low operating temperature of 150 °C. The high sensitivity has been attributed to the quasi physisorptive interactions between the polar NO_2 gas molecule and the near-stoichiometric tungsten oxide nanosheets, in which the physisorption charge transfer mechanism allows the operating temperature to be lower than the conventional chemisorptive MOx based gas sensors.[14, 65] Kadir et al.[13] have developed nanoporous WO_3 films with high sensitivity toward hydrogen and ethanol operating at temperature of 200 °C due to large surface-to-volume ratio and porosity of the film.

MOx requires some activation energy to activate surface chemical reactions for gas sensing that can be provided by applying heat. However, heating at elevated temperatures deteriorate the nanostructure of sensing material by grain growth. Another approach is photo-activation (UV irradiation) which results in enhanced sensing response with no or minimal material deterioration.[66] Photo-excitation has already resulted in remarkable response at lower temperatures (<100 ℃) for thin film and nanostructured gas sensors. For example, SnO_2 thin film has shown a response of 51% in UV irradiation for 3 ppm of NO_2 at 100 ℃ and 30% RH with a response/recovery time of 10 min/20 min,[67, 68] In_2O_3 thin film has shown a response of 0.32 and 28 for 100 ppm of CO and 3 ppm of NO_2 at room temperature in UV irradiation, respectively,[69] ZnO thin film has shown a response in the range of (52.6–49.7%) for 50 ppm of H_2O_2 with response/recovery time of 115 s/130 s,[70] and TiO_2 shown a response of 80% to 250 ppm of NO_2 with a response recovery time of 100 s/210 s at room temperature.[71] Chen et al [72] has also reported that under solar light irradiation, NiO–ZnO nanoheterojunction networks show a strong and selective response to acetone and ethanol (≈10 ppb) at room temperature. A response of 0.77 (I_{ETOH}/I_{air}-1) toward 10 ppb Ethanol has been recorded. However, the photo-excitation of electrospun nanofibers has scarcely been reported. Au-doped ZnO NFs have exhibited a response increased from 0.12 to 0.31 with the help of UV irradiation to 5 ppm ethanol at room temperature.[73]

In this work, for the first time to the best of our knowledge we present a simple and facile method to synthesize porous WO_3 NFs by electrospinning polyvinylpyrrolidone (PVP) solution containing WO_3 NPs followed by annealing as well as their applications for UV assisted acetone sensing. The PVP NFs embedded with WO_3 NPs (PVP/WO_3 composite NFs) have been annealed with slow ramp rate using two steps annealing in air. The PVP serves as a template in sintering process of WO_3 nanoparticles in nanofibrous morphology. The slow ramp rate along with a 15 minutes stay time at 300 ℃ have found to be the most critical steps in obtaining nanofibrous morphology. The porous WO_3 NFs are characterized using SEM, TEM, XRD, FTIR and XPS. Amperometric response (reaction current with analyte) of the porous WO_3 NFs has been investigated for different concentrations (1.8 – 12.5 ppm) of acetone against several applied bias voltages (3 – 7 V). Influence of different bias voltage on sensing response is also evaluated that could be an additional parameter for distinguishing the individual sensor response when multiple sensors module is used. Furthermore, the effect of photo-excitation on sensing performance and mechanism are also evaluated.

Experimental

Sample Preparation. All the chemicals in analytical grade were purchased from Sigma–Aldrich and used without any further purification. 30% w/v of WO_3 NPs (average size of 90 – 120 nm) were dispersed in ethanol for 60 min using ultrasonic stirring. Then, 20% w/v of PVP (Mw 1300,000) powder was added into that WO3 dispersion and stirred magnetically at 1000 rpm for 4 hours at room temperature. The prepared electrospinning dispersion was loaded into 1 ml plastic syringe with 21 G blunt faced stainless-steel needle. A laboratory designed electrospinning setup equipped with high voltage power supply (SRS-PS375, +20KV) was used for synthesizing PVP/WO_3 composite NFs at room temperature. The feed rate was controlled by a syringe pump (NE-1000 New Era Pump Systems, Inc.). The PVP/WO_3 composite NFs were directly electrospun

View Article Online
DOI: 10.1039/C8TC05983A

onto silicon substrates or aluminium foil for material characterizations.

Material Characterization. Microstructure and surface morphology of the PVP/WO_3 composite NFs as well as the porous WO_3 NFs were observed by field emission-scanning electron microscope (FE-SEM Ziess Sigma) equipped with energy dispersive X-ray (EDX) spectroscopy and high-resolution transmission electron microscope (HRTEM, Joel-2100F). The mean fiber diameter and fiber distribution were determined by measurements performed on 50 nanofibers using ImageJ® software.[74] The crystal structure of porous WO_3 NFs was measured by X-ray diffraction (XRD, Rigaku D/Max-2550 PC) with a Cu Ka (l ¼ 1.5406 Å) in the 2θ range of 0º – 60º. Diffraction peaks of the crystalline phase were compared with the standard compounds reported in the PDF4+ Data Files. The functional groups were identified by FTIR analysis of PVP/WO_3 NFs. The elemental composition and chemical bonding states of the porous WO_3 NFs were analyzed by Kratos AXIS Supra photoelectron spectrometer. All the spectra were charge-calibrated with C 1s peak at 286.4 eV.

Gas sensor fabrication and measurements. The sensors were developed by electrospinning PVP/WO_3 composite NFs directly on interdigitated electrodes (IDEs) followed by annealing in horizontal tube furnace in air at flow rate of 125 sccm (mL/min) to obtain porous WO_3 NFs. The IDEs were prepared from gold electrodes on alumina substrate consisting of four fingers with an interspacing of 200 µm and finger width of 300 µm. The schematic diagram of the specific electrospinning process, developed sensors and SEM images of PVP/WO_3 composite NFs and porous WO_3 NFs are shown in Fig. 1.

A multi-channel gas flow system is used for sensing measurements of porous WO_3 NFs. A G-sized cylinder containing 25 ppm of acetone balanced in air is used. Gas testing chamber was designed and built with Teflon containing a quartz window to allow UV irradiation on porous WO_3 NFs during sensing experiments. The acetone and dry air are flushed through the gas testing chamber during exposure and recovery time, respectively for 5 minutes with a constant flow rate of 200 sccm at a constant operating temperature.A 365 nm UV LED source (intensity 2.024 mW/cm^{-2}) with a 60 W/m^2 output power (Edmon Optics) was placed at a distance of ~1.5 cm from sensor for light assisted acetone sensing. The irradiation intensity was controlled by monitoring the bias current supplied to the UV-LED at a fixed distance between the UV source and sensor. PM16-140 power meter from THORLAB was used to calibrate UV LED in a dark chamber. The operating temperature was controlled using a voltage control ceramic heater (2 cm × 2 cm). The heater was able to generate a temperature ranging from 45 °C to 350 °C against a potential variation of 1.0 V to 24.0. Though, the temperature varied few degrees higher than the designed temperature value during the external bias voltage experiments, but the exact operating temperature at the sensor surface was identified using a K-type thermocouple. The sensor was stabilized in dry air at operating temperature for two hours prior to acetone sensing experiments. The amperometric response of the sensor was measured by applying different bias voltages (3 V, 5 V, and 7 V) and measuring the resulting current (µA) through the sensor in air (I_a) and in gas (I_g) environment using Kithley 2400 source meter. The time required to reach 90% of the response signal of the equilibrium value of adsorption/desorption phase of a sensing event is defined as response time (T_{res}) and recovery time (T_{rec}), respectively. Sensing repeatability is calculated as:[75]

$$\text{Repeatability (\%)} = 100\% - \text{CoV} \quad (1)$$

where CoV is coefficient of variance.

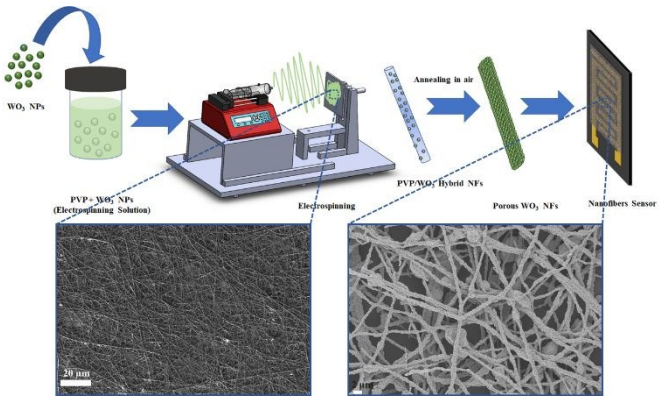

Fig. 1 Schematic illustration of porous WO_3 NFs based sensor fabrication process and SEM images of the developed NFs.

Results and discussion

Structural and morphological characterization. High surface to volume ratio of porous WO_3 NFs is required for higher gas sensitivity that is achieved by controlling their mean fiber diameter. To obtain high surface to volume ratio, electrospinning parameters were optimized using different range of voltage (7 – 15 KV), feed rate (0.1 – 0.6 ml/hr), and tip to collector distance (10 – 20 cm). Effect of electrospinning parameters on mean fiber diameter of PVP/WO_3 composite NFs is presented in Table S1, Supplementary Information (SI). Fig. S1 (SI) shows fiber diameter distribution of PVP/WO_3 samples selected from Table S1. The mean fiber diameter decreases from ~1800 nm to ~1000 nm with an increase in electrospinning voltage from 9 KV to 15 KV (Fig. S1(a, a'), SI) whereas, the mean fiber diameter reduces from ~1600 nm to ~1400 nm with an increase in tip to collector distance from 12 cm to 16 cm for voltage of 10 KV and a feed rate of 1.2 ml/hr. The fiber distribution also shifts toward lower fiber diameter with increasing tip to collector distance (Fig. S1(b, b'), SI). On the other hand, feed rate also has significant effect on the mean fiber diameter ((Fig. S1(c, c'), SI), however it is found most crucial electrospinning parameter for the bead reduction. The bead formation is effectively suppressed by adjusting the feed rate to make a stable Taylor cone against an applied electrospinning voltage. In general, the distance between needle tip and collector is found to be the most significant parameter affecting the mean fiber diameter, whereas the feed

rate and applied voltage have significant effect on the bead formation.

SEM image and fiber diameter size distribution of PVP/WO_3 composite NFs at optimum electrospinning parameters (least number of beads) are shown in the Fig. S2(a, b), SI. Most of the nanofibers are in the range of 800 – 1200 nm. EDX analysis (Fig. S3, SI) confirms the elemental composition of the PVP/WO_3 NFs deposited on Si wafer. W peaks verifies the presence of WO_3 nanoparticles embedded in PVP nanofiber. The presence of WO_3 NPs in the PVP/WO_3 composite NFs has been evaluated by FTIR (Fig. S4, SI). The spectra obtained from the nanofibers represents several strong band structures in the region of 1150 – 1750 cm^{-1} and a broad feature in the range of 500 – 1000 cm^{-1}. The characteristic bands suggest the presence of WO_3 nanoparticles within PVP in composite nanofiber. The υ(O-W-O) = 732 cm^{-1}, 793 cm^{-1}, 815 cm^{-1}, and 841 cm^{-1}, whereas υ(W-O-W) = 647 cm^{-1}, and 574 cm^{-1}. The characteristic bands in the range of 1002 – 1215 cm^{-1} represents the υ(C-N) mode. The δ(C=O) = 1228 – 1316 cm^{-1}, and δ(CH_3 or CH_2) = 1373 – 1493 cm^{-1}. The υ(C=O) = 1652 cm^{-1}. The υ(O – H) = 3289 cm^{-1} whereas υ(C – H) = 2950 cm^{-1}. The υ and δ are symbolized for stretching and bending mode of the polyatomic molecules.[24, 35] FTIR spectra of porous WO_3 NFs after annealing only showed υ(O-W-O) and υ(W-O-W) modes which shows the complete removal of polymer from the porous WO_3 NFs.

To obtain porous WO_3 NFs, annealing parameters were optimized in a two-step annealing process (Fig. S5, SI). The stay time at 300 ºC and 500 ºC was 15 min and 90 min, respectively. The ramp rate had a significant effect on morphology of the annealed WO_3 NFs. Fig. S5 (SI) shows the SEM images of annealed PVP/WO_3 NF samples at various annealing parameters given in Table S2. The nanofibrous morphology was only obtained at a ramp rate of 2 °C/min. A slow ramp rate helped in bringing WO_3 nanoparticles closer and sinter them together. There is not much reduction in fiber diameter as usually observed in nanofibers prepared from sol-gel method because the fibers are formed by the arranged sintering of nanoparticles already present in the polymer fiber. SEM images after annealing and fiber diameter distribution of developed WO_3 NFs are shown in Fig. S2(c, d), SI. WO_3 nanofiber diameter remains in the range of 900 – 1200 nm after annealing. The beads in the size of (2 – 3 µm) are seen in the WO_3 NFs. These beads are the clumps of WO_3 nanoparticles that could not be breakdown into individual particles by ultrasonic stirring in electrospinning solution preparation process. These agglomerations are not broken down even with a long ultrasonic stirring time (60 min). The SEM images of the WO_3 NFs show the rough and porous surface morphology of the fibers composed of WO_3 NFs sintered together. The micropores are also visible between individual WO_3 NFs resulting in easy diffusion of the target gas through the nanofibrous sensing layer.

Crystal structure of the porous WO_3 NFs studied by XRD is shown in Fig. 2a. The XRD pattern matches well with the triclinic WO_3 (PDF4 card number 00-032-1395) with lattice parameters a = 7.305Å, b = 7.534Å, c = 7.693Å, α = 89.848°, β = 90.587°, and γ = 89.849°. The high intensity peaks at 2θ = 23.09, 23.56, and 24.35 corresponds to the index planes (0 0 2), (0 2 0) and (2 0 0) of triclinic WO_3. The polycrystalline structure of the WO_3 nanofibers is indexed at corresponding peaks by crystal planes (0 2 -1), (1 -2 -1), (0 2 2), (2 0 2), (1 2 2), (2 2 2), (3 0 2), (2 -3 -1), (3 1 -2), (1 1 4), (0 0 4), (0 4 0), (4 0 0), (2 0 -4), (0 2 -4), (0 4 -2), and (2 -1 4). TEM images of the porous WO_3 nanofibers (Fig. 3) reveal that these nanofibers are composed of WO_3 nanoparticles sintered together. The high resolution TEM also verifies the crystallographic structure of WO_3 NFs. These WO_3 NFs have porous and highly crystalline structure with a triclinic structure with an interplanar distance of 0.164 Å, 0.385 Å, 0.262 Å, 0.269 Å, and 0.205 Å which corresponds to (2 -1 4), (0 0 2), (2 0 2), (0 2 2), and (3 0 2) crystal planes, respectively.

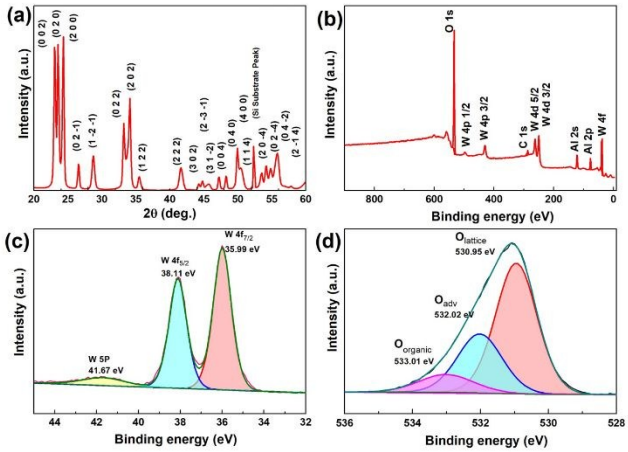

Fig. 2 (a) XRD analysis of porous WO_3 NFs. XPS analysis of porous WO_3 NFs electrospun on Al foil: (b) survey spectra; and (c – d) high resolution elemental spectra.

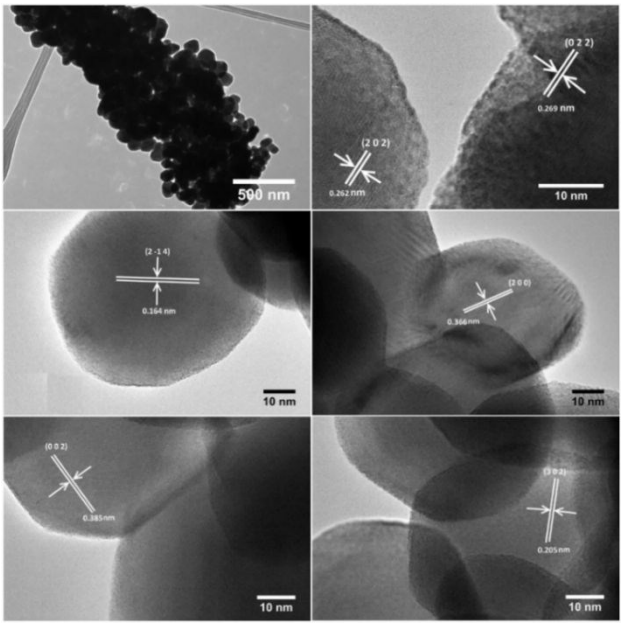

Fig. 3 TEM and HRTEM images of porous WO_3 NFs.

To confirm the chemical composition and bonding state of the porous WO_3 NFs, XPS analysis have been performed. A survey XPS spectrum confirms the existence of three components i.e. W, O, C and Al. Al appears because of the

View Article Online
DOI: 10.1039/C8TC05980J

substrate (Al foil) as shown in Fig. 2b. The high resolution XPS spectrum of WO_3 NFs near W4f peaks exhibits two distinctive peaks (spin orbit components) at the binding energies of 35.99 eV for 4f 7/2 and 38.11 eV for 4f 5/2, which correspond to the typical binding energies of W^{6+} oxidation states in WO_3 (Fig. 2c). The splitting of the 4f doublets is 2.12 eV that indicates the valence state of W is +6. Three different types of oxygen states are found on the surface. The characteristic peaks of O 1s has been convoluted into three components by using Gaussian fitting. The peak at binding energies of 530.95 eV is attributed as lattice oxygen O^{2-}. The second and third peaks at binding energy at 532.02 eV and 533.01 eV are attributed as oxygen deficient peak O^- and chemically absorbed oxygen O_2^- at the surface of WO_3 NFs (Fig. 2d). The high-resolution spectrum of C 1s has a main peak near 284.8 eV. The C 1s peak is deconvoluted into three components, the first peak at 284.8 eV is corresponds to C – C bond. The second peak at 286.58 eV corresponds to C – O groups, whereas the third peak at 288.99 eV is attributed as C = O peak (Fig. S7a, SI). The high-resolution aluminum spectra show two components of aluminum peak, first at 74.74 eV that corresponds to elemental aluminum and second at 75.14 eV corresponds to oxidized Al foil due to annealing process (Fig. S7b, SI).

Gas sensing performance and mechanism. The developed porous WO_3 NFs have been used as sensing materials in an amperometric acetone sensor. The effect of photo-activation (UV intensity of 2024 $\mu W.cm^{-2}$) on sensing performance of porous WO_3 NFs are evaluated toward various concentrations of acetone at several applied bias voltages. Sensing experiments have been performed at optimal operating temperature of 350 ℃ with further photo-activation by UV light. Table S3 (SI) shows the overall sensing behavior of porous WO_3 NFs biased at 3 V at different operating temperatures up to 350 °C. Dynamic responses of the sensor biased at 7 V toward acetone at 250 ℃ and 350 ℃ are shown in Fig. S8 (a, b) (SI), respectively. UV-LED with an emission peak centered at 365 nm is used for the photo-activation. Time dependent amperometric response of the sensor with and without UV irradiation at 350 ℃ is presented in Fig. 4(a, b). The sensor shows an n-type sensing behavior with higher response under UV irradiation. A maximum response of 1.79 µA is observed under UV irradiation compared with 1.70 µA in dark toward 12.5 ppm acetone at bias voltage of 7 V. As shown in Fig. 4c, at higher concentrations of acetone and lower bias voltage (3 V), the photo-activated response is lower than without photo-activation because of recombination of the photo-generated electrons and holes. Whereas at higher bias voltage photo-generated electrons might have higher electric force pulling more electrons through the circuit. The photo-current rises when the acetone (as a reducing gas) is injected in the sensing chamber and attain saturated level after ~24 sec at 3 V bias voltage and then returns to the original baseline current when the air is purged through the chamber. A higher magnitude of photo-current is obtained by increasing the applied voltage with a maximum photo-current at 7 V with longer response time of ~33 s. The sensor is exposed to acetone for 5 minutes followed by 5 minute purging of dry air. The developed sensor shows a recovery time of 36 sec for 3 V bias voltage under photo-activation that increases to 38 sec and 42 sec for 5 V and 7 V, respectively. Photo-activation helps exciting valance electrons to conduction band, thus enhancing the charge carrier density; therefore, increases the concentration of chemisorbed oxygen species (O_2^-, O^-, O^2) resulting in higher reaction rate with analyte gas and higher reaction current. On the other hand, it also energizes adsorbing and desorbing molecules on the WO_3 NFs surface, resulting fast adsorption and desorption kinetics.[76] Response time (T_{res}) and recovery time (T_{rec}) toward 12.5 ppm of acetone at 350 ℃ under dark and UV conditions are summarized in Table 1. The higher applied voltages (5 V and 7 V) further help analyte reaction current to draw through circuit representing even higher magnitude of response with increasing bias voltage.

A sensing mechanism is proposed and illustrated in Fig. 5. The change in reaction-current is a result of adsorption/desorption of the analyte gas and its interaction with the chemisorbed oxygen on the surface of the porous WO_3 NFs. Chemisorbed oxygen species play a vital role in gas sensing as an electron acceptor. It is found that oxygen in molecular (O_2^-) and atomic (O^-) forms chemisorbed on metal oxide surface at operating temperature ranging between 100 °C and 500 °C.[77] These chemisorbed oxygen species results in band banding as shown in Fig. 5. Therefore at 350 °C, adsorbed oxygen molecules on the surface of WO_3 NFs take electrons from conduction band and converts into O^- leaving behind a potential barrier (electron depletion region) at grain boundaries of WO_3. Upon exposure to a reducing gas such as acetone, the chemisorbed oxygen ions react with the gas to release the bound electrons to the conduction band, which reduce the resistance (or increase conductivity) of the sensing material by reducing the potential barrier at the grain boundaries (Fig. 6).[78] Consequently, the reaction current increases as the sensor is exposed to acetone and decreases when air is flushed through the system and reaches an equilibrium level.

The reaction of acetone with chemisorbed oxygen can be explained as:

$$O_{2\,(gas)} \leftrightarrow O_{2\,(ads)} + e^- \leftrightarrow 2O^-_{(ads)} \quad (2)$$

$$CH_3COCH_3 + 8O^- \rightarrow 3CO_2 + 3H_2O + 18e^- \quad (3)$$

Grain size has also a considerable influence on gas sensing performance. The developed WO_3 NFs, a combination of 1D nanostructures with highly porous morphology provides large surface area and available reactive sites facilitating easy gas diffusion. The grain boundaries are the sensitive sites which influence the sensing properties. In this work, these grain boundaries can be easily controlled by the diameter of the nanoparticles used as well as the annealing temperatures. During photo-activation WO_3 NFs absorb incoming photons that results in knocking out more electrons (and generating electron-hole pairs) from the valance band. These photo-generated electrons interact with more oxygen molecules converting them in chemisorbed oxygen species increasing the

View Article Online
DOI: 10.1039/C8TC05982A

oxygen adsorption capacity of the sensor compared with dark environment. This phenomenon further increases the reaction current under UV irradiation. Acetone molecules interact with these chemisorbed species and desorb them from surface leaving electrons back to conduction band thus reducing the height of electron depletion region at grain boundaries resulting in higher reaction currents compared with dark environment. On the other hand, when the air is flushed through the system the oxygen again extracts the electrons from the conduction band, increasing the depletion region and reducing the analyte current as shown in Fig. 6.

Repeatability is one of the critical performance parameters of gas sensors. Repeatability of the developed porous WO_3 NFs based sensor is calculated to be ≥ 99 % using equation (1). Repeatability test of the porous WO_3 NFs toward 12.5 ppm acetone in both dark and under light conditions at 350 °C is shown in Fig. 4(d, e). The sensor shows high repeatability with a minor reducing trend in response magnitude with increasing number of turns for 3 V and 7 V whereas, at 5 V it shows an increase in response magnitude (Fig. 4f). High repeatability might be attributed to the porous morphology of the developed porous WO_3 NFs as it facilitates adsorption/desorption. The sensor has shown stable results over 7 days as shown in Fig. S9, SI.

Sub ppm level detection is one of the major requirements of gas sensors for biomedical and environmental applications. Detection limit (L_D) of the porous WO_3 nanofibers based sensor is calculated by determining the three standard deviation of their noise profiles and applying the method described by Kabir et al.[79] The noise profiles of the sensor at 350 °C is recorded for a period of 1 hour while flushing the sensor chamber with dry air that were used later to calculate the L_D. The acetone detection limit of the porous WO_3 NFs has been summarized in Table 1. The developed sensor showed a lower detection limit of 70 ppb with photo-activation at lower bias voltage (3 V), whereas at higher bias voltages (5 V, and 7 V) sensor showed lower detection limit in dark environment. Selectivity of the developed porous WO_3 NFs sensor was tested towards acetone at 350 °C and 7 V bias voltage in an interfering environment of CO_2 and H_2O. The sensor was exposed to 12 pulses of each interfering gases (20% relative humidity at 30 °C/27.595 g/m^3 (H_2O) or 500 ppm of CO_2), and mixed gases. The selectivity profile of porous WO_3 sensor against CO_2 as interfering gas is shown in Fig. 5. As can be seen the sensor showed a normalized response of 2% response towards CO_2 and maximum response towards acetone. Normalized response magnitude is reduced to 95% when the sensor was exposed to acetone and CO_2 mixed environment. The normalized response magnitudes are shown in Fig. 5b. Cross-sensitivity of the porous WO_3 sensor was also tested against humidity (Fig. S10, SI). Normalized response of the sensor reduced to 51.4% when exposed to humidity only, whereas normalized response increased to 285% when sensor exposed to mixed acetone and humidity environment. This in an indication that acetone reaction with the developed material is favourable in humid environment. This behaviour of sensor needs to be studied in-depth and will be done in future research.

Table 2 presents a literature review on the developed acetone sensors by electrospinning different type of materials with various morphologies (e.g. NFs; NTs; HNFs; NRs; NB). These sensors are based on conductometric sensing platform and a low detection limit of 20 ppb has been reported. It is difficult to perform a direct comparison between the current work and the reports in the literature since sensing measurements were taken differently. However, the experimental results from porous WO_3 NFs are promising for acetone sensing with low detection limit of 1.8 ppm with relatively low response/recovery time.

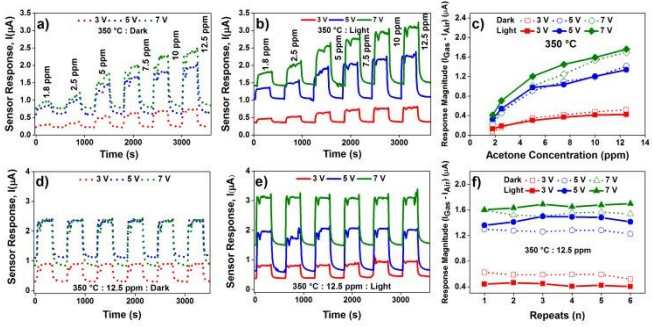

Fig. 4 Dynamic response of porous WO_3 NFs toward acetone with different concentrations and various bias voltages at 350 °C in (a) dark; (b) UV; and (c) response magnitude as a function of acetone concentration. Repeatability test of porous WO_3 NFs toward 12.5 ppm acetone at 350 °C in (d) dark and (e) UV; and (f) response magnitude.

Table 1. Response, and recovery time and detection limit of porous WO_3 NFs toward 12.5 ppm acetone at 350 °C for various bias voltages.

	T_{res} (sec)		T_{rec} (sec)		L_D (ppm)	
Bias voltage	dark	light	dark	light	dark	light
3 V	24	24	51	36	0.1	0.07
5 V	36	33	53	38	0.06	0.65
7 V	42	33	54	42	0.02	0.7

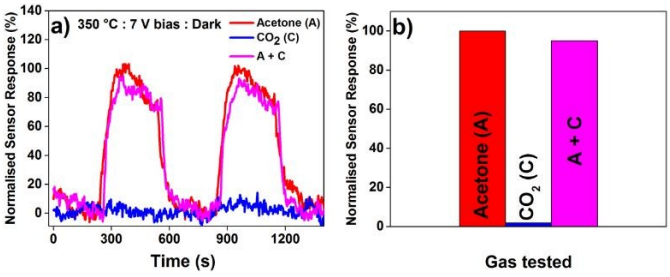

Fig. 5 (a) Selectivity profile and (b) normalized response magnitude of the porous WO_3 NFs in CO_2 as interfering gas in dark toward 12.5 ppm acetone at 350 °C.

Table 2. Acetone sensing properties of different type of electrospun nanomaterials.

Material	Morphology	Temperature [°C]	Response/acetone [ppm]	Detection limit	Response/ Recovery time	Ref
TiO_2	NRs	500	9.0/10	10 ppm	11–14 s/4–8 s	80
WO_3	NFs	270	55.6/50	0.1 ppm	6-13 s/4-9 s	6

WO_3	NTs	250	19.7/40	0.5 ppm	5 s/22 s	28
SnO_2	NBs	260	6.7/5	5 ppm	38 s /9 s	81
ZnO	HNFs	220	7.1/1	1 ppm	12–17 s/11–23 s	82
ZnO	NTs	500	12.3/2000	10 ppm	5 s/10 s	83
In_2O_3	HNFs	300	151/5	20 ppb	5 s/2 s	84
Sm-doped α-Fe_2O_3	NTs	240	33/50	500 ppb	6 s/11 s	85
Ce-doped α-Fe_2O_3	NTs	240	21.5/50	1 ppm	3 s/8 s	86
Ca-doped α-Fe_2O_3	NTs	200	24.9/100	5 ppm	1 s/3 s	87
Ce-doped ZnO	NFs	230	71.2/500	10 ppm	-	88
Ce-doped ZnO	HNFs	260	75.04/100	5 ppm	-	89
Mn-doped ZnO	NFs	340	76.2/50	50 ppm	17 s/4 s	90
Co-doped ZnO	NFs	360	16/100	5 ppm	6 s/4 s	91
La-doped ZnO	NFs	340	64/200	-	16 s/8 s	92
La_2O_3-doped WO_3	NFs	350	12.7/100	0.8 ppm	-	30
Cu-doepd WO_3	HNFs	300	6.43/20	0.25 ppm	5 s/20 s	27
Pt-doped WO_3	Hemitube	350	4.11/2	120 ppb	-	53
Eu-doped In_2O_3	NTs	240	20/20	200 ppb	3 s/90 s	93
TiO_2-SnO_2	core–shell heterostructure NFs	280	13.7/100	10 ppm	2 s/60 s	94
SnO_2–ZnO	Heterojunctions NFs	300	84/100	5 ppm	19 s/9 s	95
SnO_2/α-Fe_2O_3	NTs	200	10.07/100	5 ppm	4 s/12 s	96
SnO_2/α-Fe_2O_3	hierarchically Core-shell HNFs	340	30.363/100	2 ppm	5 s/13 s	97
a-Fe_2O_3/SnO_2	Cage-like composite NFs	275	5.3/100	100 ppm	1.5 s/2.5 s	98
ZnO–In_2O_3	Composite NTs	280	43.2/60	0.125 ppm	5 s/25 s	99
In_2O_3–Fe_2O_3	Composite NTs	240	25/100	1 ppm	3 s/7 s	100
In_2O_3–WO_3	Heterojunction NFs	275	12.9/50	0.4 ppm	6 s/64 s	29
α-Fe_2O_3 /SnO_2	Heterostructure NTs	300	33.4/100	1 ppm	4.9–5.9 s/15.8–22.5 s	101
WO_3-NiO	Heterojunction NFs	375	22.5/100	20 ppm	6 s/11 s	57
ZnO	NFs	RT	0.3μA/20	--	--	73
WO_3	Porous NFs	350	1.79 μA/12.5	1.8 ppm	33 s/42 s	This Work

NFs (nanofibers); NTs (nanotubes); HNFs (hollow nanofibers); NRs (nanorods); NB (nanobelts).

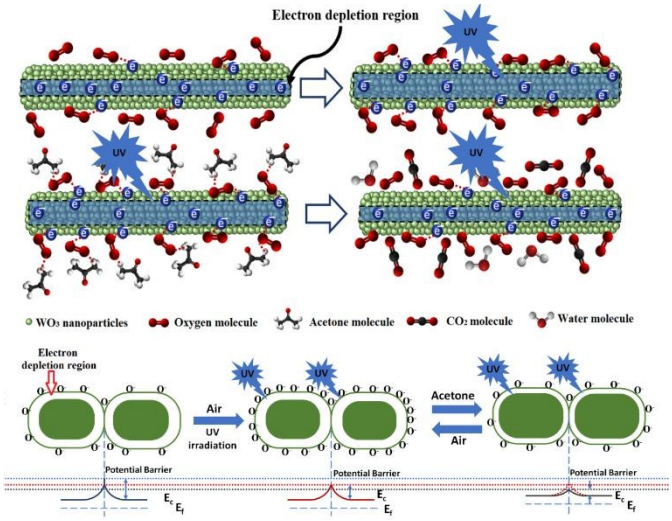

Fig. 6 Acetone sensing mechanism of the developed porous WO_3 NFs in dark and UV irradiation.

Conclusions

Highly porous WO_3 NFs were successfully synthesized using a simple technique by dispersing directly WO_3 nanoparticles (diameter of 90-120 nm) into a PVP solution followed by electrospinning and annealing. The annealing process were optimised using two steps to obtain crystalline and porous WO_3 nanofibers. SEM and TEM characterizations revealed highly porous and crystalline with a triclinic structure of WO_3 nanofibers that resulted in a highly responsive, and repeatable acetone sensor with a repeatability ≥ 99%. XRD analysis also confirmed pure triclinic WO_3 structure. Photo-activated

amperometric response of the porous WO_3 nanofibers were investigated toward acetone with various concentrations (1.8 ppm – 12.5 ppm) at different bias voltages between 3 – 7 V. A maximum photo-activated response of 1.79 µA was obtained at 7 V for 12.5 ppm acetone at optimal operating temperature of 350 °C. The developed sensor showed a sub-ppm detection limit (70 ppb) at lower bias voltage. Experimental results confirmed that the porous WO_3 nanofibers are promising for gas sensing applications including non-invasive health monitoring.

Conflicts of interest

There are no conflicts to declare.

Acknowledgements

M.S. acknowledges funding from Australian Research Council (ARC) - Discovery Project, DP150101939. M.I. would like to acknowledge QUT Postgraduate Research Award. P.S. is thankful to QUT for the financial support from the ARC for the Future Fellowship (FT130101337) and QUT core funding (QUT/ 322120-0301/07). The data reported in this paper were obtained at the Central Analytical Research Facility (CARF) operated by QUT's Institute for Future Environments.

Notes and references

1. J. Meyer, S. Hamwi, M. Kroger, W. Kowalsky, T. Riedl and A. Kahn, *Adv Mater*, 2012, **24**, 5408-5427.
2. C. Tao, S. Ruan, G. Xie, X. Kong, L. Shen, F. Meng, C. Liu, X. Zhang, W. Dong and W. Chen, *Applied Physics Letters*, 2009, **94**, 29.
3. H. Zheng, Y. Tachibana and K. Kalantar-Zadeh, *Langmuir*, 2010, **26**, 19148-19152.
4. L. Zhang, Y. Li, Q. Zhang and H. Wang, *CrystEngComm*, 2013, **15**, 5986-5993.
5. H. Lee, M. Kim, D. Sohn, S. H. Kim, S.-G. Oh, S. S. Im and I. S. Kim, *RSC Advances*, 2017, **7**, 6108-6113.
6. S. Wei, G. Zhao, W. Du and Q. Tian, *Vacuum*, 2016, **124**, 32-39.
7. R. Jiang, B. Li, C. Fang and J. Wang, *Advanced Materials*, 2014, **26**, 5274-5309.
8. T. Antonio, N. Noushin and D. Sayan, *Advanced Functional Materials*, 2017, **27**, 1605271.
9. E. Comini, *Materials Today*, 2016, **19**, 559-567.
10. J. Yu, M. Shafiei, W. Wlodarski, Y. X. Li and K. Kalantar-zadeh, *Journal of Physics D: Applied Physics*, 2010, **43**, 025103.
11. M. Shafiei, J. Yu, R. Arsat, K. Kalantar-zadeh, E. Comini, M. Ferroni, G. Sberveglieri and W. Wlodarski, *Sensors and Actuators B: Chemical*, 2010, **146**, 507-512.
12. M. Shafiei, J. Bradford, H. Khan, C. Piloto, W. Wlodarski, Y. Li and N. Motta, *Applied Surface Science*, 2018, **462**, 330-336.
13. R. Ab Kadir, W. Zhang, Y. Wang, J. Z. Ou, W. Wlodarski, A. P. O'Mullane, G. Bryant, M. Taylor and K. Kalantar-zadeh, *Journal of Materials Chemistry A*, 2015, **3**, 7994-8001.
14. H. Khan, A. Zavabeti, Y. Wang, C. J. Harrison, B. J. Carey, M. Mohiuddin, A. F. Chrimes, I. A. De Castro, B. Y. Zhang, Y. M. Sabri, S. K. Bhargava, J. Z. Ou, T. Daeneke, S. P. Russo, Y. Li and K. Kalantar-zadeh, *Nanoscale*, 2017, **9**, 19162-19175.
15. A. Staerz, U. Weimar and N. Barsan, *Sensors*, 2016, **16**, 1815.
16. S. Bai, Y. Ma, X. Shu, J. Sun, Y. Feng, R. Luo, D. Li and A. Chen, *Industrial & Engineering Chemistry Research*, 2017, **56**, 2616-2623.
17. X. Yang, V. Salles, Y. V. Kaneti, M. Liu, M. Maillard, C. Journet, X. Jiang and A. Brioude, *Sensors and Actuators B: Chemical*, 2015, **220**, 1112-1119.
18. M. Righettoni, A. Tricoli and S. E. Pratsinis, *Analytical chemistry*, 2010, **82**, 3581-3587.
19. D. Meng, T. Yamazaki, Y. Shen, Z. Liu and T. Kikuta, *Applied surface science*, 2009, **256**, 1050-1053.
20. E. Kamali Heidari, E. Marzbanrad, C. Zamani and B. Raissi, *Nanoscale research letters NRL*, 2010.
21. S. J. Choi, S. Chattopadhyay, J. J. Kim, S. J. Kim, H. L. Tuller, G. C. Rutledge and I. D. Kim, *Nanoscale*, 2016, **8**, 9159-9166.
22. J.-y. Leng, X.-j. Xu, N. Lv, H.-t. Fan and T. Zhang, *Journal of Colloid and Interface Science*, 2011, **356**, 54-57.
23. X. Lu, X. Liu, W. Zhang, C. Wang and Y. Wei, *Journal of Colloid and Interface Science*, 2006, **298**, 996-999.
24. T.-A. Nguyen, T.-S. Jun, M. Rashid and Y. S. Kim, *Materials Letters*, 2011, **65**, 2823-2825.
25. J. Sungpanich, T. Thongtem and S. Thongtem, *Materials Letters*, 2011, **65**, 3000-3004.
26. L. Giancaterini, S. M. Emamjomeh, A. De Marcellis, E. Palange and C. Cantalini, *Procedia Engineering*, 2015, **120**, 791-794.
27. X. Bai, H. Ji, P. Gao, Y. Zhang and X. Sun, *Sensors and Actuators B: Chemical*, 2014, **193**, 100-106.
28. X. Chi, C. Liu, L. Liu, Y. Li, Z. Wang, X. Bo, L. Liu and C. Su, *Sensors and Actuators B: Chemical*, 2014, **194**, 33-37.
29. C. Feng, X. Li, J. Ma, Y. Sun, C. Wang, P. Sun, J. Zheng and G. Lu, *Sensors and Actuators B: Chemical*, 2015, **209**, 622-629.
30. C. Feng, C. Wang, P. Cheng, X. Li, B. Wang, Y. Guan, J. Ma, H. Zhang, Y. Sun, P. Sun, J. Zheng and G. Lu, *Sensors and Actuators B: Chemical*, 2015, **221**, 434-442.
31. L. Giancaterini, S. M. Emamjomeh, A. De Marcellis, E. Palange, A. Resmini, U. Anselmi-Tamburini and C. Cantalini, *Sensors and Actuators B: Chemical*, 2016, **229**, 387-395.
32. H. Jane and P. T. Ralph, *Measurement Science and Technology*, 2013, **24**, 012004.
33. N.-H. Kim, S.-J. Choi, S.-J. Kim, H.-J. Cho, J.-S. Jang, W.-T. Koo, M. Kim and I.-D. Kim, *Sensors and Actuators B: Chemical*, 2016, **224**, 185-192.
34. N.-H. Kim, S.-J. Choi, D.-J. Yang, J. Bae, J. Park and I.-D. Kim, *Sensors and Actuators B: Chemical*, 2014, **193**, 574-581.
35. T.-A. Nguyen, S. Park, J. B. Kim, T. K. Kim, G. H. Seong, J. Choo and Y. S. Kim, *Sensors and Actuators B: Chemical*, 2011, **160**, 549-554.
36. X. S. Wang, G. G. Wang, H. Y. Li, L. Y. Wang, L. Liu, X. X. Guo, H. Wang and H. W. Lian, *Wuli Xuebao*, 2016, **65**.
37. D. R. Miller, S. A. Akbar and P. A. Morris, *Sensors and Actuators B: Chemical*, 2014, **204**, 250-272.
38. Q. He, Z. Zeng, Z. Yin, H. Li, S. Wu, X. Huang and H. Zhang, *Small*, 2012, **8**, 2994-2999.
39. K. Kalantar-zadeh and B. Fry, *Nanotechnology-enabled sensors*, Springer Science & Business Media, 2007.

40. E. Comini, G. Faglia and G. Sberveglieri, *Solid state gas sensing*, Springer Science & Business Media, 2008.
41. H. W. Liang, S. Liu and S. H. Yu, *Advanced Materials*, 2010, **22**, 3925-3937.
42. J.-W. Liu, H.-W. Liang and S.-H. Yu, *Chemical reviews*, 2012, **112**, 4770-4799.
43. C. L. Zhang and S. H. Yu, *Chem Soc Rev*, 2014, **43**, 4423-4448.
44. W. E. Teo and S. Ramakrishna, *Nanotechnology*, 2006, **17**, R89-R106.
45. D. Crespy, K. Friedemann and A.-M. Popa, *Macromolecular Rapid Communications*, 2012, **33**, 1978-1995.
46. S. Ramakrishna, K. Fujihara, W.-E. Teo, T. Yong, Z. Ma and R. Ramaseshan, *Materials Today*, 2006, **9**, 40-50.
47. M. Imran, N. Motta and M. Shafiei, *Beilstein Journal of Nanotechnology*, 2018, **9**, 2128-2170.
48. A. V. Stanishevsky, J. D. Wetuski and H. Yockell-Lelièvre, *Ceramics International*, 2016, **42**, 388-395.
49. J. Y. Park, K. Asokan, S.-W. Choi and S. S. Kim, *Sensors and Actuators B: Chemical*, 2011, **152**, 254-260.
50. M. Shafiei, A. Z. Sadek, J. Yu, K. Latham, M. Breedon, D. McCulloch, K. Kalantar-zadeh and W. Wlodarski, *Sensor Letters*, 2011, **9**, 11-15.
51. M. B. Rahmani, M. H. Yaacob and Y. M. Sabri, *Sensors and Actuators B: Chemical*, 2017, **251**, 57-64.
52. S.-J. Kim, S.-J. Choi, J.-S. Jang, N.-H. Kim, M. Hakim, H. L. Tuller and I.-D. Kim, *ACS nano*, 2016, **10**, 5891-5899.
53. S.-J. Choi, I. Lee, B.-H. Jang, D.-Y. Youn, W.-H. Ryu, C. O. Park and I.-D. Kim, *Analytical chemistry*, 2013, **85**, 1792-1796.
54. C. Feng, C. Wang, H. Zhang, X. Li, C. Wang, P. Cheng, J. Ma, P. Sun, Y. Gao, H. Zhang, Y. Sun, J. Zheng and G. Lu, *Sensors and Actuators B: Chemical*, 2015, **221**, 1475-1482.
55. S. J. Choi, C. Choi, S.-J. Kim, H.-J. Cho, M. Hakim, S. Jeon and I. D. Kim, *Sci. Rep.*, 2015, **5**, 8067.
56. C. Piloto, M. Shafiei, H. Khan, B. Gupta, T. Tesfamichael and N. Motta, *Applied Surface Science*, 2018, **434**, 126-133.
57. J. Zhang, H. Lu, C. Liu, C. Chen and X. Xin, *RSC Advances*, 2017, **7**, 40499-40509.
58. J. Kukkola, M. Mohl, A.-R. Leino, J. Mäklin, N. Halonen, A. Shchukarev, Z. Konya, H. Jantunen and K. Kordas, *Sensors and Actuators B: Chemical*, 2013, **186**, 90-95.
59. W.-T. Koo, S.-J. Choi, N.-H. Kim, J.-S. Jang and I.-D. Kim, *Sensors and Actuators B: Chemical*, 2016, **223**, 301-310.
60. K. H. Kim, S. J. Kim, H. J. Cho, N. H. Kim, J. S. Jang, S. J. Choi and I. D. Kim, *Sens Actuators, B Chem*, 2017, **241**, 1276-1282.
61. H. J. Cho, S. J. Kim, S. J. Choi, J. S. Jang and I. D. Kim, *Sens Actuators, B Chem*, 2017, **243**, 166-175.
62. S.-J. Kim, S.-J. Choi, J.-S. Jang, H.-J. Cho, W.-T. Koo, H. L. Tuller and I.-D. Kim, *Advanced Materials*, 2017, **29**, 1700737-n/a.
63. S. J. Choi, S. Chattopadhyay, J. J. Kim, S. J. Kim, H. L. Tuller, G. C. Rutledge and I. D. Kim, *Nanoscale*, 2016, **8**, 9159-9166.
64. S.-J. Choi, F. Fuchs, R. Demadrille, B. Grévin, B.-H. Jang, S.-J. Lee, J.-H. Lee, H. L. Tuller and I.-D. Kim, *ACS applied materials & interfaces*, 2014, **6**, 9061-9070.
65. J. Z. Ou, W. Ge, B. Carey, T. Daeneke, A. Rotbart, W. Shan, Y. Wang, Z. Fu, A. F. Chrimes, W. Wlodarski, S. P. Russo, Y. X. Li and K. Kalantar-zadeh, *ACS Nano*, 2015, **9**, 10313-10323.
66. J. Gong, Y. Li, X. Chai, Z. Hu and Y. Deng, *The Journal of Physical Chemistry C*, 2009, **114**, 1293-1298.
67. J. Saura, *Sensors and Actuators B: Chemical*, 1994, **17**, 211-214.
68. E. Comini, G. Faglia and G. Sberveglieri, *Sensors and Actuators B: Chemical*, 2001, **78**, 73-77.
69. E. Comini, A. Cristalli, G. Faglia and G. Sberveglieri, *Sensors and Actuators B: Chemical*, 2000, **65**, 260-263.
70. S. Parthasarathy, V. Nandhini and B. Jeyaprakash, *Journal of colloid and interface science*, 2016, **482**, 81-88.
71. T. Xie, N. Sullivan, K. Steffens, B. Wen, G. Liu, R. Debnath, A. Davydov, R. Gomez and A. Motayed, *Journal of alloys and compounds*, 2015, **653**, 255-259.
72. H. Chen, R. Bo, A. Shrestha, B. Xin, N. Nasiri, J. Zhou, I. Di Bernardo, A. Dodd, M. Saunders, J. Lipton-Duffin, T. White, T. Tsuzuki and A. Tricoli, *Advanced Optical Materials*, 2018, **6**, 1800677.
73. Y. Li, J. Gong, G. He and Y. Deng, *Materials Chemistry and Physics*, 2012, **134**, 1172-1178.
74. C. A. Schneider, W. S. Rasband and K. W. Eliceiri, *Nature Methods*, 2012, **9**, 671.
75. B. Lay, Y. Sabri, S. Ippolito and S. Bhargava, *Phys. Chem. Chem. Phys.*, 2014, **16**, 19522-19529.
76. N. D. Chinh, N. D. Quang, H. Lee, T. Thi Hien, N. M. Hieu, D. Kim, C. Kim and D. Kim, *Sci. Rep.*, 2016, **6**, 35066.
77. N. Barsan and U. Weimar, *Journal of Electroceramics*, 2001, **7**, 143-167.
78. I. Lee, S.-J. Choi, K.-M. Park, S. S. Lee, S. Choi, I.-D. Kim and C. O. Park, *Sensors and Actuators B: Chemical*, 2014, **197**, 300-307.
79. K. M. M. Kabir, Y. M. Sabri, G. I. Matthews, L. A. Jones, S. J. Ippolito and S. K. Bhargava, *Analyst*, 2015, **140**, 5508-5517.
80. H. Bian, S. Ma, A. Sun, X. Xu, G. Yang, J. Gao, Z. Zhang and H. Zhu, *Superlattices and Microstructures*, 2015, **81**, 107-113.
81. W. Q. Li, S. Y. Ma, J. Luo, Y. Z. Mao, L. Cheng, D. J. Gengzang, X. L. Xu and S. H. Yan, *Materials Letters*, 2014, **132**, 338-341.
82. S. Wei, M. Zhou and W. Du, *Sensors and Actuators B: Chemical*, 2011, **160**, 753-759.
83. X. Yu, F. Song, B. Zhai, C. Zheng and Y. Wang, *Physica E: Low-dimensional Systems and Nanostructures*, 2013, **52**, 92-96.
84. X. Liang, G. Jin, F. Liu, X. Zhang, S. An, J. Ma and G. Lu, *Ceramics International*, 2015, **41**, 13780-13787.
85. C. Su, C. Liu, L. Liu, M. Ni, H. Li, X. Bo, L. Liu and X. Chi, *Applied Surface Science*, 2014, **314**, 931-935.
86. C. Liu, H. Shan, L. Liu, S. Li and H. Li, *Ceramics International*, 2014, **40**, 2395-2399.
87. C. Zhao, J. Bai, B. Huang, Y. Wang, J. Zhou and E. Xie, *Sensors and Actuators B: Chemical*, 2016, **231**, 552-560.
88. G. X. Wan, S. Y. Ma, X. B. Li, F. M. Li, H. Q. Bian, L. P. Zhang and W. Q. Li, *Materials Letters*, 2014, **114**, 103-106.
89. W. Li, S. Ma, G. Yang, Y. Mao, J. Luo, L. Cheng, D. Gengzang, X. Xu and S. Yan, *Materials Letters*, 2015, **138**, 188-191.
90. Y. Sun, Z. Zhao, P. Li, G. Li, Y. Chen, W. Zhang and J. Hu, *Applied Surface Science*, 2015, **356**, 73-80.
91. L. Liu, S. Li, J. Zhuang, L. Wang, J. Zhang, H. Li, Z. Liu, Y. Han, X. Jiang and P. Zhang, *Sensors and Actuators B: Chemical*, 2011, **155**, 782-788.
92. X. L. Xu, Y. Chen, S. Y. Ma, W. Q. Li and Y. Z. Mao, *Sensors and Actuators B: Chemical*, 2015, **213**, 222-233.

View Article Online
DOI: 10.1039/C8TC05982A

93. H. Lian, G. Wang, H. Yue, L. Liu, X. Guo and X. Wang, *Micro. Nano. Lett.*, 2016, **11**, 825-827.
94. F. Li, X. Gao, R. Wang, T. Zhang and G. Lu, *Sensors and Actuators, B: Chemical*, 2016, DOI: 10.1016/j.snb.2016.12.009, 812-819.
95. S. H. Yan, S. Y. Ma, X. L. Xu, W. Q. Li, J. Luo, W. X. Jin, T. T. Wang, X. H. Jiang, Y. Lu and H. S. Song, *Materials Letters*, 2015, **159**, 447-450.
96. C. Zhao, W. Hu, Z. Zhang, J. Zhou, X. Pan and E. Xie, *Sensors and Actuators B: Chemical*, 2014, **195**, 486-493.
97. B. B. Wang, X. X. Fu, F. Liu, S. L. Shi, J. P. Cheng and X. B. Zhang, *Journal of Alloys and Compounds*, 2014, **587**, 82-89.
98. X. Li, H. Zhang, C. Feng, Y. Sun, J. Ma, C. Wang and G. Lu, *RSC Advances*, 2014, **4**, 27552-27555.
99. X. Chi, C. Liu, Y. Li, H. Li, L. Liu, X. Bo, L. Liu and C. Su, *Materials Science in Semiconductor Processing*, 2014, **27**, 494-499.
100. L. Liu, S. Li, X. Guo, Y. He and L. Wang, *Journal of Semiconductors*, 2016, **37**, 013005.
101. Q. Yu, J. Zhu, Z. Xu and X. Huang, *Sensors and Actuators B: Chemical*, 2015, **213**, 27-34.

TOC figure

View Article Online
DOI: 10.1039/C8TC05982A